Atmospheric
Chemistry
and Physics
Discussions

Open Access

Satellite observation of lowermost tropospheric ozone by multispectral synergism of IASI thermal infrared and GOME-2 ultraviolet measurements

J. Cuesta[1], M. Eremenko[1], X. Liu[2], G. Dufour[1], Z. Cai[3], M. Höpfner[4], T. von Clarmann[4], P. Sellitto[1], G. Foret[1], B. Gaubert[1], M. Beekmann[1], J. Orphal[4], K. Chance[2], R. Spurr[5], and J.-M. Flaud[1]

[1]Laboratoire Interuniversitaire des Systèmes Atmosphériques (LISA), UMR7583, CNRS, Université Paris Est Créteil, Université Paris Diderot, Créteil, France
[2]Harvard-Smithsonian Center for Astrophysics, Cambridge, Massachusetts, USA
[3]Key Laboratory of Middle Atmosphere and Global Environment Observation, Institute of Atmospheric Physics (IAP), Chinese Academy of Sciences, Beijing, China
[4]Karlsruher Institut für Technologie (KIT), Institut für Meteorologie und Klimaforschung, Karlsruhe, Germany
[5]RT Solutions Inc., Cambridge, USA

ACPD

13, 2955–2995, 2013

Lowermost tropospheric ozone by synergism of IASI and GOME-2

J. Cuesta et al.

Title Page	
Abstract	Introduction
Conclusions	References
Tables	Figures
◄◄	►►
◄	►
Back	Close
Full Screen / Esc	
Printer-friendly Version	
Interactive Discussion	

Title Page

Abstract | Introduction

Conclusions | References

Tables | Figures

|◄ | ►|

◄ | ►

Back | Close

Full Screen / Esc

Printer-friendly Version

Interactive Discussion

Abstract

We present a new multispectral approach for observing lowermost tropospheric ozone from space by synergism of atmospheric radiances in the thermal infrared (TIR) observed by IASI and earth reflectances in the ultraviolet (UV) measured by GOME-2. Both instruments are onboard the series of MetOp satellites (in orbit since 2006 and expected until 2022) and their scanning capabilities offer global coverage every day, with a relatively fine ground pixel resolution (12-km-diameter pixels spaced by 25 km for IASI at nadir). Our technique uses altitude-dependent Tikhonov-Phillips-type constraints, which optimize sensitivity to lower tropospheric ozone. It integrates the VLIDORT and KOPRA radiative transfer codes for simulating UV reflectance and TIR radiance, respectively. We have used our method to analyse real observations over Europe during an ozone pollution episode in the summer of 2009. The results show that the multispectral synergism of IASI (TIR) and GOME-2 (UV) enables the observation of the spatial distribution of ozone plumes in the lowermost troposphere (LMT, from the surface up to 3 km a.s.l., above sea level), in good quantitative agreement with the CHIMERE regional chemistry-transport model. When high ozone concentrations extend vertically above 3 km a.s.l., they are similarly observed over land by both the multispectral and IASI retrievals. On the other hand, ozone plumes located below 3 km a.s.l. are only clearly depicted by the multispectral retrieval (both over land and over ocean). This is achieved by a clear enhancement of sensitivity to ozone in the lowest atmospheric layers. The multispectral sensitivity in the LMT peaks at 2 to 2.5 km a.s.l. over land, while sensitivity for IASI or GOME-2 only peaks at 3 to 4 km a.s.l. at lowest (above the LMT). The degrees of freedom for the multispectral retrieval increase by 40 % (21 %) with respect to IASI only retrievals for atmospheric partial columns up to 3 km a.s.l. (6 km a.s.l.). Validations with ozonesondes show that our synergetic approach for combining IASI (TIR) and GOME-2 (UV) measurements retrieves lowermost tropospheric ozone with a mean bias of 2 % and a precision of 16 %, when smoothing by the retrieval vertical sensitivity (1 % mean bias and 24 % precision for direct comparisons).

Title Page

Abstract | Introduction

Conclusions | References

Tables | Figures

|◄ | ►|

◄ | ►

Back | Close

Full Screen / Esc

Printer-friendly Version

Interactive Discussion

1 Introduction

Tropospheric ozone is currently one of the air pollutants posing greatest threats to human health and ecosystems (e.g. EEA, 2011). Exposure to ground-level ozone may irritate the respiratory system, aggravate asthmas and other lung diseases and even lead to premature mortality (e.g. WHO, 2003). Air pollution's most important damages on ecosystems are produced by ozone through eutrophication and acidification, leading to yield losses and damages to agricultural crops and forests (e.g. EEA, 2011). Ozone is a strong oxidising agent that plays a central role in atmospheric photochemical processes (e.g. Seinfeld and Pandis, 1997). Tropospheric ozone is not directly emitted into the atmosphere but either formed by a chain of photochemical reactions following emissions of precursor gases near the surface (nitrogen oxides, carbon monoxide and volatile organic compounds) or transported from the stratosphere. Although emissions of most anthropogenic ozone precursors decreased substantially in the last decade in regions as Europe, this has not been reflected in observed annual average ozone concentrations (EEA, 2011).

Monitoring tropospheric ozone at the regional and global scale is a crucial societal issue. Only spaceborne remote sensing is adapted for observing tropospheric ozone at such scales. New satellite-based instruments (e.g. the Infrared Atmospheric Sounding Interferometer, IASI, onboard MetOp satellites, Clerbaux et al., 2009) offer spatial-temporal coverage particularly appropriate for monitoring air quality and for synergism with regional chemistry-transport models. For improving air quality forecasting, comprehensive pollution monitoring systems integrate satellite observations and models for inter-validation (e.g. Zyryanov et al., 2012) or for full data assimilation (e.g. Coman et al., 2012). Still, current spaceborne observations show limited sensitivity for ozone in the lowermost troposphere (LMT, here defined from the surface up to 3 km of altitude), which is the major concern for air quality. State-of-the-art methods for observing ozone mainly use spaceborne observations from only one spectral domain, either ultraviolet (UV) or thermal infrared (TIR). They are based on high spectral resolution

Title Page

Abstract | Introduction

Conclusions | References

Tables | Figures

|◄ | ►|

◄ | ►

Back | Close

Full Screen / Esc

Printer-friendly Version

Interactive Discussion

measurements in the UV from spaceborne instruments as the Global Ozone Monitoring Experiment-2 (GOME-2, see EUMETSAT, 2006) onboard MetOp-A satellite or from the Ozone Monitoring Instrument (OMI, Levelt et al., 2006) onboard the Earth Observing System-Aura, EOS-Aura satellite (using approaches as e.g. Cai et al., 2012; Liu et al., 2010) and in the TIR from IASI onboard MetOp-A, the Tropospheric Emission Spectrometer (TES, Worden et al., 2007a) onboard EOS-Aura or the Interferometric Monitor for Greenhouse gases (IMG, Kobayashi et al., 1999) instrument on the platform ADEOS (by methods like e.g. Turquety et al., 2004; Coheur et al., 2005; Kulawik et al., 2006; Eremenko et al., 2008; Dufour et al., 2012). In some cases, these approaches are used for air quality studies (e.g. Dufour et al., 2010), although they are mainly sensitive to ozone in the free troposphere (at 3 to 4 km of altitude at lowest).

A great potential for better probing lowermost tropospheric ozone from space is offered by combining the information provided by UV and TIR sounders aboard the same satellite. This is shown by simulation studies for currently in-orbit satellites like EOS-Aura (Worden et al., 2007b; Landgraf and Hasekamp, 2007) and future missions as the GEOstationary Coastal and Air Pollution Events (GEO-CAPE) satellite (Fishman et al., 2012; Natraj et al., 2011). Only very recently, a multispectral retrieval method using UV and TIR real observations of, respectively OMI and TES has shown agreement against 22 collocated ozonesonde measurements smoothed by the retrieval vertical sensitivity (with 9.7 % mean bias and 26 % precision in the LMT, Fu et al., 2012). Due to the limited spatial coverage of TES (no across-track scanning is performed), this method was analysed in a profile-to-profile basis (Fu et al., 2012).

In this paper, we present a new multispectral approach to observe lowermost tropospheric ozone using the synergy of TIR atmospheric radiances observed by IASI and UV earth reflectances measured by GOME-2. Both instruments are onboard the MetOp satellite series (in orbit since 2006 and expected until 2022 with MetOp-C) and they are both well suited for monitoring air quality at regional and global scales provided their excellent scanning capabilities. They offer global coverage every day with a relatively fine ground resolution (12-km-diameter pixels spaced by 25 km for IASI and ground pixels of

Title Page

Abstract | Introduction

Conclusions | References

Tables | Figures

|◄ | ►|

◄ | ►

Back | Close

Full Screen / Esc

Printer-friendly Version

Interactive Discussion

$80 \times 40 \, \text{km}^2$ for GOME-2, at nadir). This paper presents the capabilities of our new multi-spectral approach, so-called "IASI+GOME-2", to probe lowermost tropospheric ozone (to the authors' knowledge, the first validated method using real IASI and GOME-2 observations) and its first application for ozone pollution studies. The methodology im-
5 plemented in the multispectral scheme of IASI+GOME-2 is described in Sect. 2. The performance of IASI+GOME-2 is described in Sect. 3 in terms of (i) spectral fitting, (ii) sensitivity enhancement of the IASI+GOME-2 with respect to single-spectral-band methods and (iii) a validation against ozonesondes. Section 4 presents an analysis of IASI+GOME-2 real observations for describing an ozone pollution outbreak over Eu-
10 rope in the summer of 2009. A comparison with CHIMERE regional chemistry-transport model outputs (Sect. 4.2) confirms the capability of IASI+GOME-2 to describe the spatial distribution of lowermost tropospheric ozone plumes at the regional scale.

2 Multispectral scheme of IASI+GOME-2

The IASI+GOME-2 multispectral scheme is constructed by adapting and merging to-
15 gether two state-of-the-art and thoroughly validated methods to retrieve ozone profiles using either only IASI observations in the spectral TIR region (described by Eremenko et al., 2008, hereafter referred as "IASI" method) or only GOME-2 measurements in the UV (based on Cai et al., 2012 for forward calculations, but here with a 1/8 finer pixel resolution and a Tikhonov-Phillips-type regularization, called in the following "GOME-2"
20 retrieval). In the next sub-sections, we describe how these two methods are joined together into the IASI+GOME-2 algorithm (Sect. 2.1) and the specific developments necessary for building this multispectral inversion approach (i.e. regularization constraints and adequate fitting variables, Sects. 2.2 and 2.3).

2.1 Spectral measurements and forward simulations

For the IASI+GOME-2 approach, a so-called measurement vector y_{UV+TIR} is built up by merging together IASI TIR atmospheric radiances y_{TIR} with GOME-2 UV earth reflectances y_{UV}, i.e. $y_{UV+TIR} = [y_{UV}^T \quad y_{TIR}^T]^T$ (with ^{T} for transpose). For y_{TIR}, we use calibrated level 1C data (from e.g. http://www.pole-ether.fr/) and for y_{UV} the ratio between backscattered radiance and solar irradiance calibrated level 1B spectra (from e.g. http://www.class.ncdc.noaa.gov/). The spectral resolutions of y_{TIR} and y_{UV} are, respectively $0.5\,\mathrm{cm}^{-1}$ and $\sim 0.24\,\mathrm{nm}$ after convolution by the instrument response function and the sampling intervals are $0.25\,\mathrm{cm}^{-1}$ and $\sim 0.12\,\mathrm{nm}$. The criterion for combining IASI and GOME-2 spectra is based on the assumption that most sensitivity to ozone variability in the lowest atmospheric layers is likely provided by IASI measurements (as shown for single-band retrievals in Sects. 3.2 and 4). Thus, each IASI spectrum (12-km-diameter pixels) is matched with the co-located GOME-2 spectrum (for $80 \times 40\,\mathrm{km}^2$ pixels) without any averaging. Typically, the same y_{UV} is used 6 times with different y_{TIR}. Tropospheric ozone retrievals of IASI+GOME-2 are then calculated at the IASI ground resolution. For each IASI pixel, multispectral retrievals are processed independently (in a sequential mode).

For simulating y_{UV+TIR}, we use two radiative transfer models: the line-by-line Karlsruhe Optimized and Precise Radiative transfer Algorithm (KOPRA, Stiller et al., 2000; 2002) for y_{TIR} and the Vector Linearized Discrete Ordinate Radiative Transfer (VLIDORT, Spurr, 2006) code run in the full-polarization mode for y_{UV}. Following the IASI only approach, y_{TIR} include 7 spectral micro-windows between 980 and 1070 cm^{-1}. For y_{UV}, we consider 2 micro-windows between 290 and 345 nm accounting for the Hartley and Huggins bands (from, respectively channels 1 and 2 of GOME-2, following Cai et al., 2012). The Jacobian matrix K_{UV+TIR} is set up by putting together the Jacobians calculated by each code, i.e. $K_{UV+TIR} = [K_{UV}^T \quad K_{TIR}^T]^T$. Analytical calculations are performed for geophysical variables (atmospheric profiles and surface properties) and finite differences for instrumental parameters (shifts and corrections, see Sect. 2.2).

Title Page

Abstract | Introduction

Conclusions | References

Tables | Figures

◀ | ▶|

◀ | ▶

Back | Close

Full Screen / Esc

Printer-friendly Version

Interactive Discussion

The radiometric error matrix $\mathbf{S}_{UV+TIR}^{\varepsilon}$ contains estimations of the radiometric noise variances for each element of $\boldsymbol{y}_{UV+TIR}$. For the TIR, the noise standard deviation is taken as $20\,\text{nW}/(\text{cm}^2\,\text{cm}^{-1}\,\text{sr})$ (Eremenko et al., 2008). For the UV, noise is estimated for each wavelength using Müller matrix radiance response elements (Nowlan et al., 2011; Cai et al., 2012). Signal-to-noise ratios for GOME-2 are approximately a factor $1/\sqrt{8}$ lower than for coarser pixels considered in (Cai et al., 2012).

Ozone spectroscopic parameters used by IASI+GOME-2 are TIR atmospheric absorption line parameters taken from HITRAN 2004 (HIgh-resolution TRANsmission molecular absorption database, Rothman et al., 2005) and UV temperature-dependent cross-sections from Brion et al. (1993, hereafter BRION1993). These spectroscopic parameters are used by validated single-band approaches (Eremenko et al., 2008; Cai et al., 2012) and also in (Fu et al., 2012). Among several tests with different spectroscopic databases (see Sect. 3.3), only when using HITRAN 2004 and BRION1993 we obtain good agreement between IASI+GOME-2 retrievals in the troposphere and ozonesondes. Forward calculations consider as well the spectral signatures of H_2O and CO_2 (SO_2 and NO_2) for the TIR (UV). Except for H_2O (see Sect. 2.3), climatological profiles are taken for the other trace gases.

For all profiles, the vertical grid is set between the surface and $60\,\text{km}$ of altitude above sea level (a.s.l.), with steps of $1\,\text{km}$ up to $40\,\text{km}$ and $2\,\text{km}$ above. For each pixel, we use surface temperatures and atmospheric temperature profiles previously retrieved with KOPRA using IASI radiances (using as first guess meteorological analysis from the European Centre Medium-Range Weather Forecast, ECMWF). Following the Eremenko et al. (2008) approach, we use surface emissivity equal to unity and observations from the TIR atmospheric window ($830–950\,\text{cm}^{-1}$) for retrieving surface temperature and the CO_2 band ($700–750\,\text{cm}^{-1}$) for the temperature profile.

In the UV spectra calculations, we treat pixels with partial cloud cover as a mixture of clear sky and cloudy scenes (assumed as Lambertian surfaces with a reflectivity of $80\,\%$) according to the Independent Pixel Approximation (e.g. Cai et al., 2012) and using cloud fractions and cloud top heights (as initial values) retrieved by the FRESCO

Title Page

Abstract | Introduction

Conclusions | References

Tables | Figures

|◄ | ►|

◄ | ►

Back | Close

Full Screen / Esc

Printer-friendly Version

Interactive Discussion

algorithm (Koelemeijer et al., 2001) using GOME-2 spectra of the O_2 A band at 762 nm. As a first guess for surface albedo in the UV, we extract the OMI climatology obtained by Kleipool et al., (2008) at 347 nm. We use a single scattering rotational Raman scattering model (Sioris and Evans, 2000) for simulating the ring spectrum (filling in of solar Fraunhofer lines and telluric absorption structures by inelastic rotational Raman scattering). Using daily solar irradiance spectra observed by GOME-2, the instrument response is estimated as an asymmetric Gaussian slit function with width, shifts and asymmetric parameters adjusted for each wavelength (Cai et al., 2012) by comparison with a reference solar spectrum (Chance and Kurucz, 2010). Moreover, a "soft" recalibration is applied to each UV spectrum, which is derived on the basis of daily comparisons between measured and simulated reflectance as a function of wavelength and cross-track position (Cai et al., 2012). Aerosols are not modelled directly within VLIDORT, but their effects are partially taken into account by adjusting effective surface albedos and cloud fractions for each spectrum (Liu et al., 2010).

2.2 Retrieved variables

For each pixel, the IASI+GOME-2 retrieval scheme jointly retrieves the following state vector x_{UV+TIR},

$$x_{UV+TIR} = \left[x_{O_3}^T \ x_{H_2O}^T \ x_{offsetTIR}^T \ x_{shiftUV}^T \ x_{ringUV}^T \ x_{albedoUV}^T \ x_{cloud}^T \right]^T \tag{1}$$

Thus we obtain the ozone profile x_{O_3} (volume mixing ratios) by inverting y_{UV+TIR} and jointly adjusting the water vapour profiles x_{H_2O}, offsets $x_{offsetTIR}$ for each TIR microwindow, wavelength shifts $x_{shiftUV}$ for the UV radiance and irradiance spectra (1 per UV channel), multiplicative factors of the ring spectrum x_{ringUV} (1 per UV channel), surface albedo multiplicative factors $x_{albedoUV}$ (a constant for channel 1 of GOME-2 and 3 parameters of a 2nd degree polynomial function of wavelength for channel 2), and a factor for cloud fraction x_{cloud} used in the UV forward calculations. The multiplicative factors x_{ringUV} account for the multiple scattering contributions to the UV ring spectrum

(e.g. Liu et al., 2010; Cai et al., 2012). Offsets for each TIR micro-window are meant to compensate potential effects of partial cloud cover and aerosols in the IASI spectra (Eremenko et al., 2008; Dufour et al., 2010).

First guess and a priori values for x_{O_3} are taken from the climatology of McPeters et al., (2007). We extract one climatological x_{O_3} for mid-latitudes (averaged over 30–60° N) and one for the tropics (20–30° N). They are used alternatively for pixels with tropopause heights below 14 km a.s.l. (proxy for mid-latitudes airmasses) or above (for tropical airmasses, as done by Sellitto et al., 2012a). Tropopause heights are derived from atmospheric temperature profiles retrieved from IASI spectra. For each pixel, we interpolate ECMWF analysis for obtaining first guess profiles for x_{H_2O}. Initial values for $x_{offsetTIR}$ and $x_{shiftUV}$ are set to 0 and all multiplicative factors to 1.

2.3 Inversion and constraints

To invert y_{UV+TIR}, we implement a constrained least squares fit method using a Tikhonov-Phillips-type (Tikhonov, 1963; Kulawik et al., 2006) altitude-dependent regularization that optimizes sensitivity to lower troposphere ozone (as done for the TIR by Eremenko et al., 2008). It is numerically implemented using KOPRAFIT (the inversion module of KOPRA), adapted for the multispectral approach. The regularization matrix $R_{UV+TIR}^{O_3}$ constrains the zero, first and second order finite differences of the retrieved ozone profile, in adequacy with the information provided by y_{UV+TIR}. The strengths of the altitude-dependent constraints are a polynomial function of altitude (of 4th order), whose coefficients are derived by minimizing the following figure of merit

$$F = k_1 \frac{s_{LMT}^{tot}}{(DOF_{LMT})^N} + k_2 \frac{s_{LT}^{tot}}{(DOF_{LT})^N} + k_3 \frac{s_{TOTAL}^{tot}}{(DOF_{TOTAL})^N}. \quad (2)$$

When minimizing F, we maximize the degrees of freedom while minimizing the a posteriori total error (as done by Kulawik et al., 2006; Eremenko et al., 2008), simultaneously for several atmospheric columns. We consider the lowermost troposphere (LMT, below

2964

3 km a.s.l.), the lower troposphere (below 6 km a.s.l., indicated LT in the following) and the total column (up to 60 km a.s.l., called here TOTAL). Degrees of freedom DOF_{col} and estimates of a posteriori total errors s_{col}^{tot} are calculated for each atmospheric column (indicated generally by the subscript $_{col}$). We choose the values of the coefficients

5 $k_{1,2,3}$ and N for approximately matching s_{col}^{tot} of IASI+GOME-2 with that for IASI only (detailed as LISA product in Dufour et al., 2012).

Following Rodgers' (2000) formalism, we estimate the a posteriori total error matrix $\mathbf{S}^{tot}$ as the sum of the errors due to smoothing $\mathbf{S}^{smooth}$, measurement noise $\mathbf{S}^{mes}$, cross-state uncertainties in water vapour $\mathbf{S}_{H_2O}^{cross}$ and other fitting variables $\mathbf{S}_{param}^{cross}$ (both

10 calculated following Worden et al., 2007a) and systematic errors in carbon dioxide $\mathbf{S}_{CO_2}^{syst}$ and atmospheric temperature $\mathbf{S}_T^{syst}$ profiles used in the retrieval (other systematic errors are assumed negligible). As for TIR or UV only, $\mathbf{S}^{smooth}$ and $\mathbf{S}^{mes}$ are the principal contributions to $\mathbf{S}^{tot}$. For a partial atmospheric column col, we obtain s_{col}^{tot} as the root sum of the diagonal elements of $\mathbf{S}^{tot}$ (as done by e.g. Steck, 2002; Liu et al., 2010).

15 We use DOF_{col} to describe the sensitivity of the ozone retrieval (see Sect. 3.2), as it is the number of independent pieces of information available at each atmospheric column col from the measurements. Following Rodgers (2000), it is calculated as the trace of the so-called averaging kernel matrix $\mathbf{A}$ (also called AVK) over the range of col. The AVK matrix represents the sensitivity of the retrieval to the true atmospheric state and

20 it is calculated by a classical expression (e.g. Steck and von Clarmann, 2000; Steck, 2002), here given for matrices of the multispectral approach,

$$\mathbf{A} = \left[\mathbf{K}_{UV+TIR}^T \quad \left(\mathbf{S}_{UV+TIR}^{\varepsilon} \right)^{-1} \quad \mathbf{K}_{UV+TIR} + \mathbf{R}_{UV+TIR} \right]^{-1} \quad \mathbf{K}_{UV+TIR}^T \quad \left(\mathbf{S}_{UV+TIR}^{\varepsilon} \right)^{-1} \quad \mathbf{K}_{UV+TIR}.$$

(3)

We also characterize the height of maximum sensitivity to ozone H_{col}^{max} for the partial column col as the height of the maximum of the corresponding AVK (the sum of rows

25 of $\mathbf{A}$ for col). The constraints for the elements of $\boldsymbol{x}_{UV+TIR}$ (except for $\boldsymbol{x}_{O_3}$ and $\boldsymbol{x}_{H_2O}$) are

taken as 1 over the variance of each parameter. The adjustment of x_{H_2O} is included in the IASI+GOME-2 scheme in order to avoid aberrant retrievals of x_{O_3} at the LT, which are obtained when the variability of H_2O is not properly considered. For x_{H_2O}, we use zero and first order constraints proportional to 1 over the variance of water vapour at each altitude (calculated from a 5 yr climatology of radiosoundings at Paris).

In the following sections, all ozone retrievals use Tikhonov-Phillips-type regularization adapted for each spectral domain: $\mathbf{R}^{O_3}_{UV+TIR}$ for IASI+GOME-2, $\mathbf{R}^{O_3}_{UV}$ for GOME-2 only (also obtained by minimizing Eq. (2) but with $\mathbf{y}_{UV}$, $\mathbf{K}_{UV}$, $\mathbf{S}^{\varepsilon}_{UV}$ and $\mathbf{x}_{UV}$ in Eqs. 1 and 3) and $\mathbf{R}^{O_3}_{TIR}$ for IASI only (used by Eremenko et al., 2008; Dufour et al., 2012). For the 3 cases, a posteriori error estimates $\mathbf{S}^{tot}$ are kept approximately similar. This leads to weaker multispectral ozone constraints in $\mathbf{R}^{O_3}_{UV+TIR}$ than for single-band retrievals and it provides with a greater number of degrees of freedom than when using $\mathbf{R}^{O_3}_{UV}$ or $\mathbf{R}^{O_3}_{TIR}$. Note that IASI+GOME-2 also gains sensitivity when using the same regularization matrix as for single-band retrievals (but less than with $\mathbf{R}^{O_3}_{UV+TIR}$) through the complementarity of UV and TIR measurements to describe the vertical distribution of ozone.

3 Performance of IASI+GOME-2

3.1 Multiple spectral fitting

As mentioned in Sect. 2, the IASI+GOME-2 measurement vector $\mathbf{y}_{UV+TIR}$ integrates coincident GOME-2 reflectances and IASI radiances (see an example in Fig. 1a). Different orders of magnitude in the intensities of the spectra and the measurement noise are present for shorter (channel 1) and longer (channel 2) UV wavelengths and TIR wavenumbers (Fig. 1 plots the successive elements in $\mathbf{y}_{UV+TIR}$ and vertical dashed lines separate the 3 spectral regions). The IASI+GOME-2 approach simultaneously fits the whole $\mathbf{y}_{UV+TIR}$ within the uncertainties of each element, after 4 iterations. For

pixels with low cloud fraction ($< 30\%$), typical root-mean-square (RMS) spectral residuals between observed and fitted spectra are $\sim 6.5\%$ and $\sim 0.20\%$ for, respectively the shorter and longer UV wavelengths and $\sim 0.35\%$ for TIR wavenumbers. Residuals are mostly random (see examples in Fig. 1b) and systematic features (only slightly

5 apparent for longer UV wavelengths) remain within the order of magnitude of the radiometric noise. These levels of fitting residuals are reached for all pixels shown in Sect. 3.3 (i.e. a validation against ozonesondes) and Section 4 (i.e. regional analyses of IASI+GOME-2 retrievals). Moreover, the horizontal distribution of fitting residuals is mostly homogeneous for clear-sky pixels, without any particularities for $\boldsymbol{y}_{UV+TIR}$

10 constructed with different $\boldsymbol{y}_{TIR}$ and the same $\boldsymbol{y}_{UV}$ (neither seen for IASI+GOME-2 retrievals, see Sect. 4).

3.2 Sensitivity enhancement to lowermost tropospheric ozone

The combination of the UV and TIR measurements in the IASI+GOME-2 approach allows a significant enhancement of sensitivity to ozone over the whole atmospheric

15 column (see Table 1). The total column DOF_{TOTAL} for IASI+GOME-2 is typically ~ 5.2 (in average over land), thus $\sim 50\%$ higher than for IASI or GOME-2 only retrievals. For the lowest atmospheric layers, a remarkable sensitivity gain is as well observed for IASI+GOME-2 with respect to single-band retrievals. Both over land and over ocean, the mean DOF_{LMT} for IASI+GOME-2 is higher by at least 40% than for IASI only (a factor

20 tor 3 higher than for GOME-2 only, see Table 1). This is illustrated in Figure 2, which shows a comparison between typical AVKs up to 12 km a.s.l. for IASI+GOME-2 (red), IASI (green) and GOME-2 (blue) over land (top) and ocean (bottom). For the multi-spectral retrieval, a clear increase and shift of sensitivity (higher AVK values) towards the lowest layers of the troposphere is clearly depicted (particularly for the LMT over

25 land, see Fig. 2a). In the example over land, IASI+GOME-2 AVKs for the lowest layers peak around 2 km a.s.l. (Fig. 2a), thus 1 km below those for IASI (Fig. 2b) and 2 km below the ones for GOME-2 (Fig. 2c). Both over land and over ocean, we may notice 2 semi-independent partial columns (two relative peaks, one up to 6 km a.s.l. and

Title Page

Abstract | Introduction

Conclusions | References

Tables | Figures

|◄ | ►|

◄ | ►

Back | Close

Full Screen / Esc

Printer-friendly Version

Interactive Discussion

a second one from 6 to 12 km a.s.l.) for IASI+GOME-2 (Fig. 2a and d). Except for IASI over land (Fig. 2b), the AVKs of the other single-band cases show a single large peak in the troposphere (see Fig. 2c, e and f).

Figures 3 quantify these features in terms of DOF_{col} and H_{col}^{max} for all partial columns from the surface up to each vertical level within the LT (from 1 up to 6 km a.s.l., in average of land and ocean pixels over Europe for 19–20 August 2009). The relative gain of degrees of freedom is significantly higher for vertical levels closer to the surface. Over land, the DOF_{col} for IASI+GOME-2 are 77 %, 40 % and 21 % higher than for IASI (and higher than a factor 3 with respect to GOME-2, Fig. 3a) for, respectively the partial columns up to 1 km a.s.l., 3 km a.s.l. (LMT) and 6 km a.s.l. (LT). The mean DOF_{LMT} for IASI+GOME-2 is ∼ 0.34 (Table 1), thus in the same order of magnitude as for the joint retrieval with TES and OMI (∼ 0.37 up to 700 hPa which is at 3 km a.s.l. in a standard atmosphere, Fu et al., 2012).

For all partial columns in the LT, the height of maximum sensitivity H_{col}^{max} of IASI+GOME-2 is 800–900 m below that for IASI both over land and over ocean (and 1.3 km below that for GOME-2 over land, see Fig. 3b, d). Sensitivity maxima for IASI and GOME-2 are at lowest at 3.0 and 3.7 km above ground level (a.g.l.). In this case, averaging kernels for all levels within the LMT peak above the LMT top height. For IASI+GOME-2, sensitivity peak height H_{LMT}^{max} over land is located in average at ∼ 2.2 km a.g.l. (Table 1), thus within the LMT partial column itself. Over ocean, IASI+GOME-2 sensitivity within the LT peaks at similar heights as for GOME-2 (3.4 to 3.8 km a.s.l., Fig. 3d) but with DOF_{LT} a factor 2.6 higher.

Figure 4 presents the geographical distribution of DOF_{LT} and H_{LT}^{max} over Europe for 19 August 2009. The gain of sensitivity of IASI+GOME-2, both for DOF_{LT} and H_{LT}^{max}, is consistently observed over the whole continent (Fig. 4). Sensitivity dependence between land and ocean is apparent for IASI only and also for IASI+GOME-2 retrievals, due to different thermal contrasts (differences between the temperature of the surface and the lowest atmospheric layer). Over ocean, where IASI only LT sensitivity peaks around 6 km a.g.l., IASI+GOME-2 performance is similar that for IASI over land (both

for DOF_{LT} and H_{LT}^{max}, see also Table 1). For GOME-2 only (Fig. 4e), sensitivity changes less between land and ocean, but with regional enhancements of DOF_{LT} likely depending on the ozone vertical distribution (e.g. around 45–50° N 20° E and 38–45° N 8° W in Figs. 4e and 7e). Higher spatial variability is observed for H_{LT}^{max} (Fig. 4, right panels) than for DOF_{LT} (Fig. 4, left panels), depending on the atmospheric and surface conditions. For southern (western) European regions over land as Spain (France), relatively high (moderate) surface temperatures and thermal contrasts of 11.5 K (2.4 K) induce H_{LT}^{max} of ∼ 1.9 km a.g.l. (∼ 2.8 km a.g.l.) for IASI+GOME-2 whereas ∼ 2.4 km a.g.l. (∼ 3.8 km a.g.l.) for IASI only.

For the LMT partial column (see Fig. 5), the sensitivity enhancement of IASI+GOME-2 with respect to IASI is more marked than for the LT over the whole continent. For IASI+GOME-2, H_{LMT}^{max} is located in average at 2.2 km a.g.l., 400 m below H_{LT}^{max} and in all cases over land within the LMT. In Spain (France), H_{LMT}^{max} for IASI+GOME-2 reaches ∼ 1.6 km a.g.l. (∼ 2.6 km a.g.l.). For the single-band approaches, the heights of maximum sensitivity for the LMT and LT partial columns are practically the same and above the LMT upper boundary at 3 km a.s.l. (Fig. 4d, and 5d).

Note that all calculations of the AVK matrices account for all variables in the state vector (including all instrumental parameters, see Eq. 1). Indeed, if we had neglected the uncertainties of the parameters different from ozone (as sometimes done in sensitivity studies), we would have obtained a significant overestimation of the degrees of freedom (e.g. 37 % in the LMT) and underestimations of the sensitivity height (e.g. by 500 m for the LMT).

3.3 Validation against ozonesondes

In this sub-section, we analyse the quality of the IASI+GOME-2 ozone retrieval by comparison with reference ozonesonde measurements. We consider all ozonesondes provided by the World Ozone and Ultraviolet radiation Data Centre (WOUDC, http://www.woudc.org) for the summer 2009 from 10 different launching sites (spread from 40° N to 60° N): Ankara (Turkey), De Bilt (Holland), Hohenpeissenberg (Germany),

Legionowo (Poland), Lerwik (Scotland), Lindenberg (Germany), Madrid (Spain), Payerne (Switzerland), Uccle (Holland) and Valentia (Ireland). The accuracy of the ozone concentration measurement is expected to reach ±5 % (Deshler et al., 2008), as most ozonesondes use the electrochemical concentration cell technique (except for Hohenpeissenberg with Brewer Mast sondes). Ozonesonde profiles have a vertical resolution of about ∼ 150 m and typically extend from the surface up to 30 km a.s.l. For the comparison, we follow the methodology used for validating several IASI scientific ozone products (Keim et al., 2009; Dufour et al., 2012). Coincidence criteria are spatial co-localization within ±110 km and a time frame of 7 h from the MetOp-A morning over-pass (at 09:30 LT). We only use IASI+GOME-2 pixels with low cloud fraction (< 30 %) that pass a series of quality checks (for discarding unphysical and aberrant retrievals). The comparison is made for each ozonesonde with the average of collocated satellite retrievals.

The IASI+GOME-2 validation results are summarized in Tables 2 and 3. The number of days with coincident IASI and GOME-2 pixels with ozonesondes is 57 and the number of ozonesondes after screening cloudy scenes is 119. Tables 2 and 3 consider, respectively ozonesonde profiles vertically smoothed by convolution with each IASI+GOME-2 AVK matrix and "raw" ozonesonde measurements. Both comparisons show good agreement between IASI+GOME-2 retrievals and ozonesondes, with very similar results as for the IASI only retrieval for mid-latitudes (see LISA product in Dufour et al., 2012). Accounting for the retrieval sensitivity (Table 2), the mean bias of the multispectral retrievals in the LT is −4 %, the RMS difference is below 18 % and the correlation coefficient R is 0.7 (see scatter plot in Fig. 6a). Integrated ozone up to 30 km a.s.l. (named UPTO30) agrees with ozonesondes with a mean bias of −1.8 %, RMS below 6 % and 0.93 of correlation. Only a slightly higher mean bias (−7.5 %) is observed for the TROPO (up to 12 km a.s.l.). For the LMT, the IASI+GOME-2 retrievals show a good performance with a relatively high linear correlation (0.87), a low bias (−2.1 %) and similar RMS (17 %) with respect to smoothed ozonesondes (see Table 2 and Fig. 6b). Direct comparisons with raw ozonesondes (Table 3) show that the mean

Title Page

Abstract | Introduction

Conclusions | References

Tables | Figures

|◀ | ▶|

◀ | ▶

Back | Close

Full Screen / Esc

Printer-friendly Version

Interactive Discussion

biases of IASI+GOME-2 retrievals also remain very low without smoothing by the retrieval sensitivity (below 1 % in the LMT and below 4 % in the LT, see Table 3 and Figs. 6c, d). As expected by the influence of the smoothing error, linear correlations (0.75 in the LMT and 0.58 in the LT) and RMS (24 % in the LMT and 20 % in the LT) are
slightly degraded (with respect to Table 2). Table 3 shows that RMS differences with raw ozonesondes are generally greater than a posteriori error estimates s_{col}^{tot}, as they also include errors in the ozonesondes ($\sim$ 5 %) and ozone variability within the spatial-temporal coincidence criteria (or due to eventual underestimations of s_{col}^{tot}). For the LMT and LT, RMS differences for direct comparisons (Table 3) are consistent with the sum
of the smoothing error s_{col}^{smooth} and the RMS differences with smoothed ozonesondes (see Tables 2 and 3, the root sum of variances is 2.4 DU and 4.4 DU for, respectively the LMT and the LT). Subtracting the variance from ozonesonde errors, we estimate a precision of the IASI+GOME-2 retrievals in the LMT of 23.7 % for direct comparisons and 15.7 % when smoothing by the retrieval sensitivity. Moreover, a posteriori total errors s_{col}^{tot} remain as low as the ones for IASI only (see Dufour et al., 2012), as expected from the design of the multispectral retrieval constraints (Sect. 2.3).

Table 4 presents additional tests on the potential effects on the multispectral ozone retrieval due to inconsistencies in the UV/TIR spectroscopic parameters. According to laboratory studies, spectral discrepancies between UV cross-sections databases and TIR line intensities (e.g. HITRAN 2004) may reach 4 to 5 % (Picquet-Varrault et al., 2005; Gratien et al., 2010). The consequences of such incompatibilities are not straightforward, since several fitting parameters modify the absolute calibration of the spectra (i.e. TIR spectral offsets, fitting effective UV surface albedos and UV soft recalibration). Thus, we verify the overall effects by comparing ozonesonde measurements (119 sondes) with the multispectral ozone retrieval either using HITRAN 2000 (with TIR line intensities approximately +4 % higher than HITRAN 2004) or changing the UV cross-sections by −5 %. The results in Table 4 indicate that these changes in the spectroscopic databases induce negative (−2.5% for HITRAN 2000) and positive (1.5 % with −5 % UV cross-sections) corrections for the UPTO30 partial column (partially including

Title Page

Abstract | Introduction

Conclusions | References

Tables | Figures

|◄ | ►|

◄ | ►

Back | Close

Full Screen / Esc

Printer-friendly Version

Interactive Discussion

the stratospheric ozone layer). However, aberrant retrievals are obtained in the tro-posphere for both corrections. Table 4 shows strong negative biases in the LMT, LT and TROPO (between −10 % and −19 %), higher RMS and much lower linear correla-tions. Among the tested databases, only HITRAN 2004 and BRION1993 enable a good match between the IASI+GOME-2 approach and ozonesondes (shown in Tables 2 and 3).

4 Lowermost tropospheric ozone observed by IASI+GOME-2

In this section, we illustrate the capacities of the IASI+GOME-2 multispectral approach to characterize ozone pollution events at the regional scale. We analyse LT and LMT ozone observations for a typical ozone pollution outbreak over Europe during sum-mer. It is a moderate ozone event, mainly occurring on 19 and 20 August 2009 (also analysed by Sellitto et al., 2012a). Surface ozone concentrations occasionally reached 90 ppb (the ozone information threshold, e.g. EEA, 2011). It occurs during typical sum-mer anticyclonic conditions and relatively high surface temperatures over Western Eu-rope (Foret et al., personal communication, 2013).

First, we describe the ozone pollution event as seen by different satellite observa-tions (Sect. 4.1). Then, we compare IASI+GOME-2 observations with the state-of-the-art regional chemistry-transport model CHIMERE (Schmidt et al., 2001; Bond et al., 2007) in Sect. 4.2. This comparison verifies the inter-consistency of IASI+GOME-2 and CHIMERE for describing the spatial distribution of ozone plumes and it illustrates the potential of IASI+GOME-2 for evaluating air quality models or for data assimilation (e.g. Zyryanov et al., 2012; Coman et al., 2012). CHIMERE runs with a horizontal reso-lution of 0.25° × 0.25° and 17 vertical levels from the surface up to 200 hPa. It is driven by ECMWF meteorological analysis and it uses boundary conditions every 3 h, supplied by the global model MOZART (Model for Ozone and Related chemical Tracers, Horowitz et al., 2003; Emmons et al., 2010). CHIMERE outputs for 19–20 August 2009 have been exhaustively validated against surface and ozonesonde measurements, showing

Title Page

Abstract | Introduction

Conclusions | References

Tables | Figures

|◀ | ▶|

◀ | ▶

Back | Close

Full Screen / Esc

Printer-friendly Version

Interactive Discussion

very similar agreement as obtained for previous studies (Zyryanov et al, 2012). For the comparison, we use CHIMERE outputs at 10:00 UTC.

4.1 Satellite retrieval of LT ozone

Figure 7 shows LT ozone retrievals by IASI+GOME-2 (top), IASI (middle) and GOME-2 (bottom) for the 2 days of the ozone pollution event. The main ozone pollution plume over Western Europe is consistently observed over land by both IASI and IASI+GOME-2. On 19 August, it is located over Spain (centred at 38° N 5° W) and France (44–50° N 0–5° E). The day after, it is observed over Germany and Denmark (49–55° N 10° E) following an eastward travelling meteorological front originating from the Atlantic (see the white cloudy band over UK, 55° N 2° W). This ozone plume is not clearly made evident by GOME-2 only retrievals, as may be expected due to its small sensitivity in the LT (see Table 1). IASI+GOME-2 observations show slightly higher (3–10 %) ozone concentrations within the plume than detected by IASI. Note that both observations are not directly comparable due to differences in the AVKs. The larger values for IASI+GOME-2 are consistent with the sensitivity gain in the lowest layers, which enables the observation of higher ozone concentrations produced near the surface.

The multispectral retrieval IASI+GOME-2 (Figs. 7a, b) shows additional LT ozone plumes both over land and over ocean, which are not clearly depicted by the single-band approaches (Figs. 7c–f). Over ocean, this is the case over the Mediterranean (Fig. 7a particularly north-east of Italy, 42° N 3° E), over the Atlantic (45° N 3° W), over the North Sea (55° N 3° E) and over the Black Sea (45° N 30° E). This retrieval also enables the observation of a continuous structure of high ozone concentration zones between ocean and land (e.g. on 19 August over the Atlantic, the North Sea and the Black Sea). Over land, only IASI+GOME-2 clearly depicts an ozone plume over Eastern Europe (e.g. Fig. 7a over Poland and Hungry, 45–52° N 20° E). It is consistently seen on both days (moving eastwards) and for 2 successive MetOp-A overpasses on each day. In this region (47° N 22° E), IASI retrievals show a weak concentration increase within the background variability and less marked than the western plume over

ACPD

13, 2955–2995, 2013

Lowermost tropospheric ozone by synergism of IASI and GOME-2

J. Cuesta et al.

Title Page

Abstract	Introduction
Conclusions	References
Tables	Figures

Back | Close

Full Screen / Esc

Printer-friendly Version

Interactive Discussion

Spain and France (Fig. 7c, d). GOME-2 retrievals suggest high ozone concentrations for the Northeastern part of the plume (50° N 20–35° E, Fig. 7e, f).

4.2 Comparison of IASI+GOME-2 with simulated LMT ozone

Figures 8 and 9 present a comparison of IASI+GOME-2 (Figs. 8a and 9a) ozone partial columns in the LMT (up to 3 km a.s.l.) and the corresponding CHIMERE outputs (smoothed by the IASI+GOME-2 AVKs in Figs. 8b and 9b). A remarkable overall agreement in the ozone plume structures is observed for the 2 days of the pollution event. The Western (over France and Spain on 19 August) and Eastern (over Poland and Hungry on 19 August) ozone plumes over land are both depicted with very similar structures in the observed and simulated LMT ozone columns. A particularly good agreement is seen for the shape of the ozone plumes on the west and southwest of France and west of Spain (Figs. 8a–c). According to CHIMERE outputs without smoothing, the Eastern plume over Hungry (47° N 22° E) is located below 3 km a.s.l. (in the LMT, see Figs. 8c and 9c). This is consistent with the fact that this plume is clearly made evident only by IASI+GOME-2 (on both days). On 20 August, ozone plumes shift eastwards (Fig. 9). Both CHIMERE simulations and IASI+GOME-2 observations show higher ozone concentrations below 3 km a.s.l. at the centre of the ozone plume over Northern Germany and Denmark (50–55° N 6° E in Fig. 9a–c).

Over sea surfaces, the ozone plumes only seen by IASI+GOME-2 are simulated by CHIMERE, over the Mediterranean, the Atlantic, the Black Sea and the North Sea (see Fig. 8c). Particularly, high concentrations observed by IASI+GOME-2 over the Mediterranean are also indicated by CHIMERE in the LMT (see CHIMERE RAW Surface – 3 km a.s.l., Figs. 8c and 9c). The ocean-land continuity of the plumes over the Atlantic and the Black Sea (Fig. 8) is clearly identified by CHIMERE and IASI+GOME-2. Interestingly, also large sea-land gradients between the Adriatic Sea and Italy as well as Western Mediterranean and Spain appear both in IASI+GOME-2 LMT observations and in smoothed CHIMERE simulations. Theses differences are both due to

larger LMT ozone concentrations over the sea and to larger sensitivities over land than over sea.

In terms of absolute ozone concentrations, IASI+GOME-2 (Figs. 8a and 9a) and CHIMERE outputs smoothed by IASI+GOME-2 sensitivity (Figs. 8b and 9b) show a general good agreement (mean bias below 1 % over the whole region). Some differences in the background concentrations (around 1 to 2 DU) are observed locally, as expected by the uncertainties in both data. In general, IASI+GOME-2 ozone columns show more horizontal variability, which could be linked to retrieval noise ($s_{\text{LMT}}^{\text{tot}}$ is ~ 2 DU) or also possibly to smoothed model outputs.

According to CHIMERE raw outputs (Figs. 8d and 9d), the ozone plumes reaching altitudes between 3 and 6 km a.s.l. correspond to the ones clearly observed over land by both IASI and IASI+GOME-2 (i.e. the Western ozone plume in Fig. 7). Since DOF_{LMT} for IASI+GOME-2 is lower than 1, multispectral outputs in the LMT (Figs. 8a and 9a) are expected to depend as well on ozone concentrations up to 5 or 6 km a.s.l. (see AVKs over land of Fig. 2). Thus, IASI+GOME-2 retrievals alone cannot tell whether the ozone plumes are located in the LMT or between 3 and 6 km a.s.l. However, one may identify ozone plumes located below 3 km a.s.l. as they are clearly depicted by IASI+GOME-2, but not by IASI.

5 Summary and perspectives

We have presented a new multispectral approach IASI+GOME-2 to observe ozone in the lowermost troposphere, by combining the information provided by IASI (TIR) and GOME-2 (UV) spaceborne observations. The information content enhancement for IASI+GOME-2 enables an increase of sensitivity to ozone in the whole atmospheric column and especially below 3 km a.s.l. (LMT), which is particularly valuable for ozone pollution studies. Sensitivity in the LMT shows a striking enhancement of at least 40 % (in terms of DOF_{LMT}), with a relative maximum peaking on average at 2.2 km a.g.l. over land (thus at least 800 m below than the single-band methods). Validation against

ozonesondes shows low biases (2 % and 4 %) and relatively good linear correlations (0.87 and 0.70) for the tropospheric columns up to 3 and 6 km a.s.l. (LMT and LT). Ozone plumes reaching altitudes above 3 km a.s.l. (according to CHIMERE model simulations) are consistently depicted over land by both IASI+GOME-2 and IASI only. The unique capacity of IASI+GOME-2 is the observation of ozone plumes located below 3 km a.s.l. (LMT) both over land and over ocean. This is a major step-forward in spaceborne remote sensing of lowermost tropospheric ozone and its application for air quality studies.

A further improvement for detection of near-surface ozone is expected by including the information provided by the Chappuis band in the visible (VIS) spectrum (Chance et al., 1997). The advantages of a combined UV+VIS retrieval of ozone have been experimentally confirmed with real satellite observations by a neural network approach (Sellitto et al., 2012b,c). Future works for further improvement of the IASI+GOME-2 approach will focus on a three-band multispectral retrieval UV+VIS+TIR.

Title Page

Abstract | Introduction

Conclusions | References

Tables | Figures

|◄ | ►|

◄ | ►

Back | Close

Full Screen / Esc

Printer-friendly Version

Interactive Discussion

References

Blond, N., Boersma, K. F., Eskes, H. J., van der A, R. J., Van Roozendael, M., De Smedt, I.,
  Bergametti, G., and Vautard, R.: Intercomparison of SCIAMACHY nitrogen dioxide observa-
  tions, in situ measurements and air quality modeling results over Western Europe, J. Geo-
  phys. Res., 112, D10311, doi:10.1029/2006JD007277, 2007.
Brion, J., Chakir, A., Daumont, D., Malicet, J., and Parisse, C., : High-resolution labora-
  tory absorption cross section of O_3: temperature effect, Chem. Phys. Lett., 213, 610–612,
  doi:10.1016/0009-2614(93)89169-I, 1993.
Cai, Z., Liu, Y., Liu, X., Chance, K., Nowlan, C. R., Lang, R., Munro, R., and Suleiman, R.:
  Characterization and correction of Global Ozone Monitoring Experiment 2 ultraviolet mea-
  surements and application to ozone profile retrievals?, J. Geophys. Res., 117, D07305,
  doi:10.1029/2011JD017096, 2012.
Chance, K. and Kurucz, R. L.: An improved high-resolution solar reference spectrum for Earth's
  atmosphere measurements in the ultraviolet, visible, and near infrared, J. Quant. Spectrosc.
  Ra., 111, 1289–1295, doi:10.1016/j.jqsrt.2010.01.036, 2010.
Chance, K. V., Burrows, J. P., Perner, D., and Scheider, W.: Satellite measurements of at-
  mospheric ozone profiles, including tropospheric ozone, from ultraviolet/visible measure-
  ments in the nadir geometry: a potential method, J. Quant. Spectrosc. Ra., 57, 467–476,
  doi:10.1016/S0022-4073(96)00157-4, 1997.
Clerbaux, C., Boynard, A., Clarisse, L., George, M., Hadji-Lazaro, J., Herbin, H., Hurtmans, D.,
  Pommier, M., Razavi, A., Turquety, S., Wespes, C., and Coheur, P.-F.: Monitoring of atmo-
  spheric composition using the thermal infrared IASI/MetOp sounder, Atmos. Chem. Phys., 9,
  6041–6054, doi:10.5194/acp-9-6041-2009, 2009.

Title Page

Abstract | Introduction

Conclusions | References

Tables | Figures

|◄ | ►|

◄ | ►

Back | Close

Full Screen / Esc

Printer-friendly Version

Interactive Discussion

Coheur, P. F., Barret, B., Turquety, S., Hurtmans, D., Hadji-Lazaro, J. and Clerbaux, C. : Retrieval and characterization of ozone vertical profiles from a thermal infrared nadir sounder, J. Geophys. Res., 110, D24303, doi:10.1029/2005JD005845, 2005.

Coman, A., Foret, G., Beekmann, M., Eremenko, M., Dufour, G., Gaubert, B., Ung, A., Schmechtig, C., Flaud, J.-M., and Bergametti, G.: Assimilation of IASI partial tropospheric columns with an Ensemble Kalman Filter over Europe, Atmos. Chem. Phys., 12, 2513–2532, doi:10.5194/acp-12-2513-2012, 2012.

Deshler, T., Mercer, J. L., Smit, H. G. J., Stubi, R., Levrat, G., Johnson, B. J., Oltmans, S. J., Kivi, R., Thompson, A. M., Witte, J., Davies, J., Schmidlin, F. J., Brothers, G., and Sasaki, T.: Atmospheric comparison of electrochemical cell ozonesondes from different manufacturers, and with different cathode solution strengths: the Balloon Experiment on Standards for Ozonesondes, J. Geophys. Res., 113, D04307, doi:10.1029/2007JD008975, 2008.

Dufour, G., Eremenko, M., Orphal, J., and Flaud, J.-M.: IASI observations of seasonal and day-to-day variations of tropospheric ozone over three highly populated areas of China: Beijing, Shanghai, and Hong Kong, Atmos. Chem. Phys., 10, 3787–3801, doi:10.5194/acp-10-3787-2010, 2010.

Dufour, G., Eremenko, M., Griesfeller, A., Barret, B., LeFlochmoën, E., Clerbaux, C., Hadji-Lazaro, J., Coheur, P.-F., and Hurtmans, D.: Validation of three different scientific ozone products retrieved from IASI spectra using ozonesondes, Atmos. Meas. Tech., 5, 611–630, doi:10.5194/amt-5-611-2012, 2012.

Emmons, L. K., Walters, S., Hess, P. G., Lamarque, J.-F., Pfister, G. G., Fillmore, D., Granier, C., Guenther, A., Kinnison, D., Laepple, T., Orlando, J., Tie, X., Tyndall, G., Wiedinmyer, C., Baughcum, S. L., and Kloster, S.: Description and evaluation of the Model for Ozone and Related chemical Tracers, version 4 (MOZART-4), Geosci. Model Dev., 3, 43–67, doi:10.5194/gmd-3-43-2010, 2010.

Eremenko, M., Dufour, G., Foret, G., Keim, C., Orphal, J., Beekmann, M., Bergametti, G., and Flaud, J.-M.: Tropospheric ozone distributions over Europe during the heat wave in July 2007 observed from infrared nadir spectra recorded by IASI, Geophys. Res. Lett., 35, L18805, doi:10.1029/2008GL034803, 2008.

European Environment Agency: Air quality in Europe – 2011 report, EEA Technical report 12/2011, Publications Office of the European Union, ISSN 1725–2237, doi:10.2800/83213, 2011.

Lowermost tropospheric ozone by synergism of IASI and GOME-2

J. Cuesta et al.

Title Page

Abstract	Introduction
Conclusions	References
Tables	Figures

|◄ ►|

◄ ►

Back Close

Full Screen / Esc

Printer-friendly Version

Interactive Discussion

European Organisation for the Exploitation of Meteorological Satellites (EUMETSAT): GOME-2 Level 1 product generation specification, EPS.SYS.SPE.990011, Darmstadt, Germany, 2006.

Fishman, J., Iraci, L. T., Al-Saadi, J., Chance, K., Chavez, F., Chin, M., Coble, P., Davis, C., DiGiacomo, P. M., Edwards, D., Eldering, A., Goes, J., Herman, J., Hu, C., Jacob, D. J., Jordan, C., Kawa, S. R., Key, R., Liu, X., Lohrenz, S., Mannino, A., Natraj, V., Neil, D., Neu, J., Newchurch, M., Pickering, K., Salisbury, J., Sosik, H., Subramaniam, A., Tzortziou, M., Wang, J., and Wang, M.: The United States' next generation of atmospheric composition and coastal ecosystem measurements: NASA's Geostationary Coastal and Air Pollution Events (Geo-Cape) Mission, B. Amer. Meteorol. Soc., 93, 1547–1566, 2012.

Fu, D., Worden, J. R., Liu, X., Kulawik, S. S., Bowman, K. W., and Natraj, V.: Characterization of ozone profiles derived from Aura TES and OMI Radiances, Atmos. Chem. Phys. Discuss., 12, 27589–27636, doi:10.5194/acpd-12-27589-2012, 2012.

Gratien, A., Picquet-Varrault, B., Orphal, J., Doussin, J.-F., and Flaud, J.-M.: New laboratory intercomparison of the ozone absorption coefficients in the mid-infrared (10 µm) and ultraviolet (300–350 nm) spectral regions, J. Phys. Chem. A, 114, 10045–10048, 2010.

Horowitz, L. W., Walters, S., Mauzerall, D. L., Emmons, L. K., Rasch, P. J., Granier, C., Tie, X., Lamarque, J.-F., Schultz, M. G., Tyndall, G. S., Orlando, J. J., and Brasseur, G. P.: A global simulation of tropospheric ozone and related tracers: description and evaluation of MOZART, version 2, J. Geophys. Res., 108, 4784, doi:10.1029/2002JD002853, 2003.

Keim, C., Eremenko, M., Orphal, J., Dufour, G., Flaud, J.-M., Höpfner, M., Boynard, A., Clerbaux, C., Payan, S., Coheur, P.-F., Hurtmans, D., Claude, H., Dier, H., Johnson, B., Kelder, H., Kivi, R., Koide, T., López Bartolomé, M., Lambkin, K., Moore, D., Schmidlin, F. J., and Stübi, R.: Tropospheric ozone from IASI: comparison of different inversion algorithms and validation with ozone sondes in the northern middle latitudes, Atmos. Chem. Phys., 9, 9329–9347, doi:10.5194/acp-9-9329-2009, 2009.

Kleipool, Q. L., Dobber, M. R., de Haan, J. F., and Levelt, P. F.: Earth surface reflectance climatology from 3 years of OMI data, J. Geophys. Res., 113, D18308, doi:10.1029/2008JD010290, 2008.

Kobayashi, H., Shimota, A., Kondo, K., Okumura, E., Kameda, Y., Shimoda, H. and Ogawa, T., Development and evaluation of the interferometric monitor for greenhouse gases: a high-throughput Fourier-transform infrared radiometer for nadir Earth observation, Appl. Opt., 38, 6801–6807, 1999.

Title Page

Abstract | Introduction

Conclusions | References

Tables | Figures

|◄ | ►|

◄ | ►

Back | Close

Full Screen / Esc

Printer-friendly Version

Interactive Discussion

Koelemeijer, R., Stammes, P., Hovenier, J., and Haan, J. D.: A fast method for retrieval of cloud parameters using oxygen A band measurements from the Global Ozone Monitoring Experiment, J. Geophys. Res., 106, 3475–3490, doi:10.1029/2000JD900657, 2001.

Kulawik, S. S., Osterman, G., Jones, D. B. A., and Bowman, K. W.: Calculation of altitude-dependent Tikhonov constraints for TES nadir retrievals, IEEE T. Geosci. Remote, 44, 1334–1342, 2006.

Landgraf, J. and Hasekamp, O. P.: Retrieval of tropospheric ozone: the synergistic use of thermal infrared emission and ultraviolet reflectivity measurements from space, J. Geophys. Res., 112, D08310, doi:10.1029/2006JD008097, 2007.

Levelt, P. F., van den Oord, G. H. J., Dobber, M. R., Mälkki, A., Visser, H., de Vries, J., Stammes, P., Lundell, J., and Saari, H.: The Ozone Monitoring Instrument, IEEE T. Geosci. Remote, 44, 1093–1101, 2006.

Liu, X., Bhartia, P. K., Chance, K., Spurr, R. J. D., and Kurosu, T. P.: Ozone profile retrievals from the Ozone Monitoring Instrument, Atmos. Chem. Phys., 10, 2521–2537, doi:10.5194/acp-10-2521-2010, 2010.

McPeters, R. D., Labow, G. J., and Logan, J. A.: Ozone climatological profiles for satellite retrieval algorithms, J. Geophys. Res., 112, D05308, doi:10.1029/2005JD006823, 2007.

Natraj, V., Liu, X., Kulawik, S., Chance, K., Chatfield, R., Edwards, D. P., Eldering, A., Francis, G., Kurosu, T., Pickering, K., Spurr, R., Worden, H.: Multispectral sensitivity studies for the retrieval of tropospheric and lowermost tropospheric ozone from simulated clear sky GEO-CAPE measurements. Atmos. Environ., 45, 7151–7165, doi:10.1016/j.atmosenv.2011.09.014, 2011.

Nowlan, C. R., Liu, X., Chance, K., Cai, Z., Kurosu, T. P., Lee, C., and Martin, R. V.: Retrievals of sulfur dioxide from the Global Ozone Monitoring Experiment 2 (GOME-2) using an optimal estimation approach: algorithm and initial validation, J. Geophys. Res., 116, D18301, doi:10.1029/2011JD015808, 2011.

Picquet-Varrault, B., Orphal, J., Doussin, J.-F., Carlier, P., and Flaud, J.-M.: Laboratory intercomparison of the ozone absorption coefficients in the mid-infrared (10 μm) and ultraviolet (300–350 nm) spectral regions, J. Phys. Chem. A, 109, 1008–1014, doi:10.1021/jp0405411, 2005.

Rodgers, C. D.: Inverse Methods for Atmospheric Sounding: Theory and Practice, World Scientific Publishing Company, London, UK, 2000.

Rothman, L. S., Jacquemart, D., Barbe, A., Chris Benner, D., Birk, M., Brown, L. R., Carleer, M. R., Chackerian Jr., C., Chance, K., Coudert, L. H., Dana, V., Devi, V. M., Flaud, J.-M., Gamache, R. R., Goldman, A., Hartmann, J.-M., Jucks, K. W., Maki, A. G., Mandin, J.-Y., Massie, S. T., Orphal, J., Perrin, A., Rinsland, C. P., Smith, M. A. H., Tennyson, J., Tolchenov, R. N., Toth, R. A., Vander Auwera, J., Varanasi, P., and Wagner, G.: The HITRAN 2004 molecular spectroscopic database, J. Quant. Spectrosc. Ra., 96, 139–204, 2005.

Sellitto, P., Dufour, G., Eremenko, M., Cuesta, J., Dauphin, P., Forêt, G., Gaubert, B., Beekmann, M., Peuch, V.-H., and Flaud, J.-M.: Potential of the future thermal infrared spaceborne sensor IASI-NG to monitor lower tropospheric ozone, Atmos. Meas. Tech. Discuss., 5, 7025–7065, doi:10.5194/amtd-5-7025-2012, 2012a.

Sellitto, P., Del Frate, F., Solimini, D., and Casadio, S.: Tropospheric ozone column retrieval from ESA-Envisat SCIAMACHY nadir UV/VIS radiance measurements by means of a neural network algorithm, IEEE T. Geosci. Remote, 50, 998–1011, doi:10.1109/TGRS.2011.2163198, 2012b.

Sellitto, P., Di Noia, A., Del Frate, F., Burini, A., Casadio, S., and Solimini, D.: On the role of visible radiation in ozone profile retrieval from nadir UV/VIS satellite measurements: an experiment with neural network algorithms inverting SCIAMACHY data, J. Quant. Spectrosc. Ra., 113, 1429–1436, doi:10.1016/j.jqsrt.2012.04.007, 2012c.

Schmidt, H., Derognat, C., Vautard, R., and Beekmann, M.: A comparison of simulated and observed ozone mixing ratios for summer of 1998 in western Europe, Atmos. Environ., 35, 6277–6297, 2001.

Seinfeld, J. H. and Pandis, S. N.: Atmospheric Chemistry and Physics, from Air Pollution to Climate Change, John Wiley & Sons Inc., Toronto, Canada, 1997.

Sioris, C. and Evans, W.: Impact of rotational Raman scattering in the O_2 A band, Geophys. Res. Lett., 27, 4085–4088, doi:10.1029/2000GL012231, 2000.

Spurr, R. J. D.: VLIDORT: A linearized pseudo-spherical vector discrete ordinate radiative transfer code for forward model and retrieval studies in multilayer multiple scattering media, J. Quant. Spectrosc. Ra., 102, 316–342, doi:10.1016/j.jqsrt.2006.05.005, 2006.

Steck, T.: Methods for determining regularization for atmospheric retrieval problems, Appl. Opt., 41, 1788–1797, doi:10.1364/AO.41.001788, 2002.

Steck, T. and von Clarmann, T.: Constrained profile retrieval applied to the observation mode of the Michelson interferometer for passive atmospheric sounding, Appl. Opt., 40, 3559–3571, 2000.

Title Page

Abstract | Introduction

Conclusions | References

Tables | Figures

|◀ | ▶|

◀ | ▶

Back | Close

Full Screen / Esc

Printer-friendly Version

Interactive Discussion

Stiller, G. P. (Ed.) with contributions from v. Clarmann, T., Dudhia, A., Echle, G., Funke, B., Glatthor, N., Hase, F., Höpfner, M., Kellmann, S., Kemnitzer, H., Kuntz, M., Linden, A., Linder, M., Stiller, G. P., and Zorn, S.: The Karlsruhe Optimized and Precise Radiative Transfer Algorithm (KOPRA), vol. FZKA 6487 of Wissenschaftliche Berichte, Forschungszentrum Karlsruhe, Germany, 2000.

Stiller, G. P., von Clarmann, T., Funke, B., Glatthor, N., Hase, F., Höpfner, M., and Linden, A.: Sensitivity of trace gas abundances retrievals from infrared limb emission spectra to simplifying approximations in radiative transfer modelling, J. Quant. Spectrosc. Ra., 72, 249–280, doi:10.1016/S0022-4073(01)00123-6, 2002.

Tikhonov, A.: On the solution of incorrectly stated problems and a method of regularization, Dokl. Acad. Nauk SSSR, 151, 501–504, 1963.

Turquety, S., Hadji-Lazaro, J., Clerbaux, C., Hauglustaine, D. A., Clough, S. A., Cassé, V., Schlüssel, P., and Mégie, G.: Operational trace gas retrieval algorithm for the Infrared Atmospheric Sounding Interferometer, J. Geophys. Res., 109, D21301, doi:10.1029/2004JD004821, 2004.

Worden, H. M., Logan, J. A., Worden, J. R., Beer, R., Bowman, K., Clough, S. A., Eldering, A., Fisher, B. M., Gunson, M. R., Herman, R. L., Kulawik, S. S., Lampel, M. C., Luo, M., Magretskaia, I. A., Osterman, G. B., and Shephard, M. W.: Comparisons of Tropospheric Emission Spectrometer (TES) ozone profiles to ozonesondes: Methods and initial results, J. Geophys. Res., 112, D03309, doi:10.1029/2006JD007258, 2007a.

Worden, J., Liu, X., Bowman, K., Chance, K., Beer, R., Eldering, A., Gunson, M., and Worden, H.: Improved tropospheric ozone profile retrievals using OMI and TES radiances, Geophys. Res. Lett., 34, L01809, doi:10.1029/2006GL027806, 2007b.

World Health Organization (WHO): Health Aspects of Air Pollution with Particulate Matter, Ozone and Nitrogen Dioxide, Bonn, Germany, 13–15 January 2003.

Zyryanov, D., Foret, G., Eremenko, M., Beekmann, M., Cammas, J.-P., D'Isidoro, M., Elbern, H., Flemming, J., Friese, E., Kioutsioutkis, I., Maurizi, A., Melas, D., Meleux, F., Menut, L., Moinat, P., Peuch, V.-H., Poupkou, A., Razinger, M., Schultz, M., Stein, O., Suttie, A. M., Valdebenito, A., Zerefos, C., Dufour, G., Bergametti, G., and Flaud, J.-M.: 3-D evaluation of tropospheric ozone simulations by an ensemble of regional Chemistry Transport Model, Atmos. Chem. Phys., 12, 3219–3240, doi:10.5194/acp-12-3219-2012, 2012.

Title Page

Abstract | Introduction

Conclusions | References

Tables | Figures

|◄ | ►|

◄ | ►

Back | Close

Full Screen / Esc

Printer-friendly Version

Interactive Discussion

Table 1. Sensitivity of the multispectral ozone retrieval IASI+GOME-2 (UV+TIR) and comparison with IASI (TIR) and GOME-2 (UV) only retrievals. Degrees of freedom for signal and the height of maximum sensitivity (km a.g.l.) are given for different atmospheric partial columns (LMT, LT, TROPO and TOTAL are respectively from the surface up to 3, 6, 12 and 60 km a.s.l.). Statistics are given in mean values and standard deviations (with respect to the average, in parenthesis) for all pixels over land and over ocean on 19–20 August 2009 for the region shown in Fig. 4. In order to compare partial columns of similar depths, we consider only land pixels with ground altitudes below 300 m a.s.l. For these pixels, the average thermal contrast is 4.4 ± 2.4 K over land and 0.9 ± 1.5 K over ocean.

	Atmospheric column	IASI+GOME-2		IASI		GOME-2	
		Land	Ocean	Land	Ocean	Land	Ocean
Degrees of freedom for signal DOF$_{col}$	LMT	0.34 (± 0.04)	0.23 (± 0.04)	0.24 (± 0.03)	0.16 (± 0.04)	0.08 (± 0.01)	0.08 (± 0.02)
	LT	0.75 (± 0.05)	0.64 (± 0.05)	0.62 (± 0.03)	0.52 (± 0.04)	0.25 (± 0.03)	0.24 (± 0.04)
	TROPO	1.72 (± 0.07)	1.51 (± 0.12)	1.52 (± 0.06)	1.34 (± 0.09)	0.67 (± 0.04)	0.65 (± 0.05)
	TOTAL	5.20 (± 0.12)	4.92 (± 0.19)	3.43 (± 0.10)	3.20 (± 0.10)	3.41 (± 0.10)	3.32 (± 0.12)
Height of maximum sensitivity H_{col}^{max}	LMT	2.20 (± 0.50)	3.48 (± 0.56)	3.02 (± 0.67)	4.26 (± 0.51)	3.68 (± 0.50)	3.64 (± 0.65)
	LT	2.45 (± 0.55)	3.83 (± 0.57)	3.21 (± 0.70)	4.36 (± 0.53)	3.72 (± 0.46)	3.66 (± 0.64)

Table 2. Validation of IASI+GOME-2 ozone retrievals against ozonesonde measurements smoothed by IASI+GOME-2 averaging kernels. We consider 119 ozonesondes launched between June and August 2009 from 10 stations over Europe. Cloudy pixels and aberrant satellite retrievals are screened out. The comparison is expressed in Dobson Units (DU) and in percentage (in parenthesis) in terms of mean bias, root mean square differences (RMS) and linear correlation coefficients R.

Validation of IASI+GOME-2 ozone retrieval vs. ozonesondes smoothed by the retrieval AVK			
Atmospheric column	Bias	RMS	R
LMT	−0.21 (−2.1%)	1.7 (16.5%)	0.87
LT	−0.9 (−4.1%)	3.8 (17.2%)	0.70
TROPO	−3.5 (−7.5%)	7.0 (15.2%)	0.89
UPTO30	−4.6 (−1.8%)	14.8 (5.7%)	0.93

Table 3. Direct comparison of IASI+GOME-2 ozone retrievals against raw ozonesonde measurements. The same as Table 2 but without smoothing ozonesonde profiles with IASI+GOME-2 averaging kernels. We also provide estimations of the a posteriori total and smoothing errors, s_{col}^{tot} and s_{col}^{smooth}, for the IASI+GOME-2 retrievals used in the comparison.

Direct comparison of IASI + GOME-2 ozone retrieval vs. raw ozonesondes					
Atmospheric column	Bias	RMS	R	s_{col}^{tot}	s_{col}^{smooth}
LMT	−0.1 (−0.7 %)	2.4 (24.2 %)	0.75	2.0 (20.2 %)	1.8 (18.0 %)
LT	−0.7 (−3.2 %)	4.4 (20.4 %)	0.58	2.6 (12.2 %)	2.2 (10.3 %)
TROPO	−2.0 (−4.5 %)	6.9 (15.6 %)	0.86	3.8 (9.0 %)	3.3 (7.7 %)
UPTO30	−4.7 (−1.8 %)	15.4 (5.7 %)	0.92	7.4 (2.9 %)	6.2 (2.5 %)

Table 4. Evaluation of potential effects of spectroscopic incoherencies between the UV and TIR datasets on the multispectral ozone retrieval. The same comparison (119 ozonesondes smoothed by the retrieval AVKs) as in Table 2 is performed, but for 2 test cases: (left) either using TIR spectroscopic parameters from HITRAN 2000 or (right) decreasing UV cross-sections by −5 % with respect to BRION1993.

IASI+GOME-2 with HITRAN 2000/with −5 % UV cross sections vs. ozonesondes smoothed by the retrieval AVK			
Atmospheric column	Bias	RMS	R
LMT	−1.6/ − 1.2 (−14.7 %/ − 12.0 %)	2.7/2.4 (24.9 %/22.8 %)	0.69/0.78
LT	−4.3/ − 2.9 (−18.5 %/ − 13.0 %)	6.2/5.1 (26.8 %/22.9 %)	0.40/0.54
TROPO	−5.4/ − 4.4 (−10.9 %/ − 9.6 %)	8.7/7.7 (17.4 %/16.4 %)	0.85/0.88
UPTO30	−6.6/4.0 (−2.5 %/1.5 %)	16.6/14.8 (6.2 %/5.7 %)	0.91/0.93

Full Screen / Esc
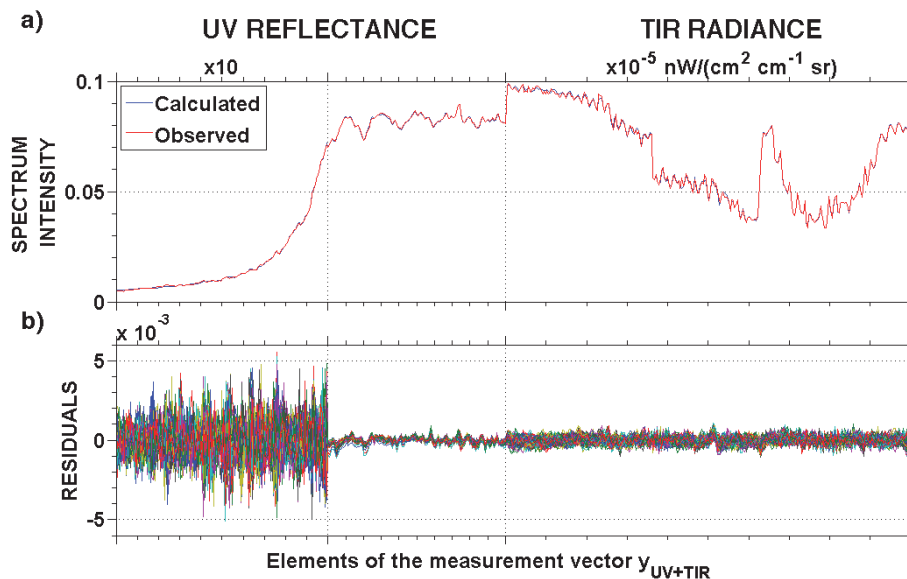
Fig. 1. Typical examples of co-localized radiance and reflectance spectra observed, respectively by IASI and GOME-2 instruments and fitted by the IASI+GOME-2 approach. **(a)** Observed (red) and calculated (blue) elements in the IASI+GOME-2 measurement vector $y_{\text{UV+TIR}}$ including UV reflectances in the Hartley (left, multiplied by 10) and Huggins (middle) bands and TIR radiances (right, divided by 10^5). **(b)** Fitting residuals of 200 typical spectra in the same units as **(a)**.
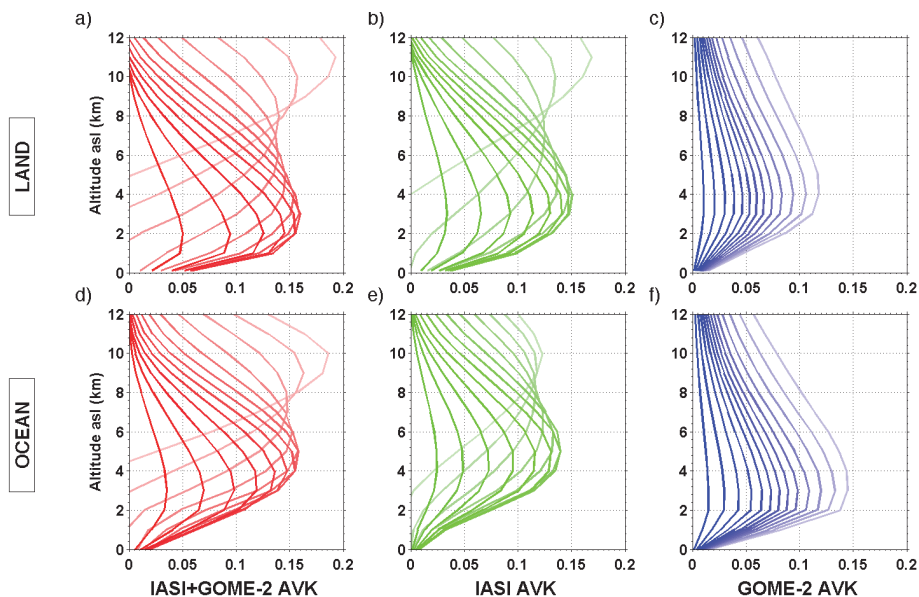
Fig. 2. Typical examples of averaging kernels (AVK) between the surface and 12 km a.s.l. for (**a** and **d**) IASI+GOME-2, (**b** and **e**) IASI only and (**c** and **f**) GOME-2 only ozone retrieval methods, over land (top) and over ocean (bottom). Lighter colours are given for AVK's rows at higher altitudes.
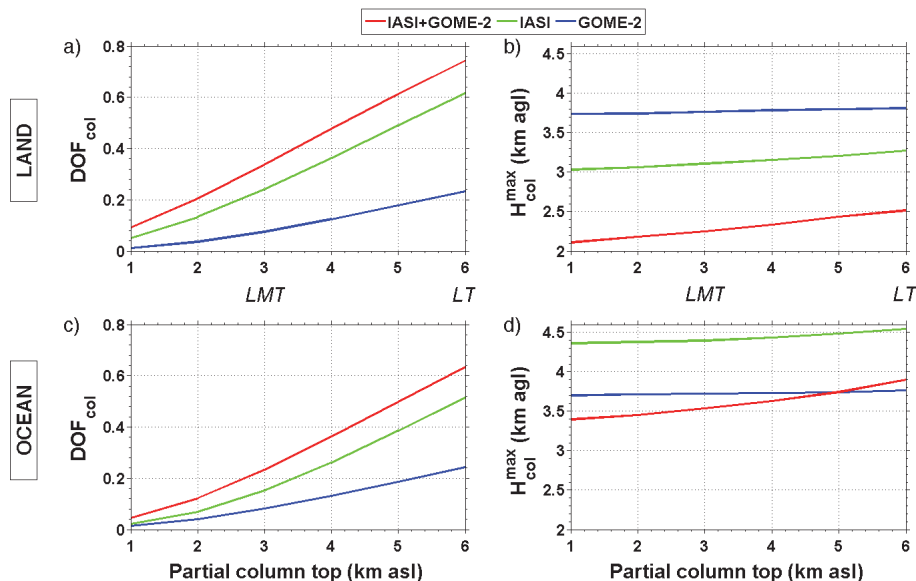
Fig. 3. Sensitivity comparison in terms of **(a,c)** degrees of freedom DOF$_{col}$ and **(b,d)** heights of maximum AVK (km a.g.l.) H^{max}_{col} for partial columns from the surface up to the altitude indicated in abscissa (from 1 to 6 km a.s.l.) for IASI+GOME-2 (red), IASI only (green) and GOME-2 (blue) ozone retrievals for an average of pixels over land (top) and over ocean (bottom) over Europe on 19–20 August 2009.
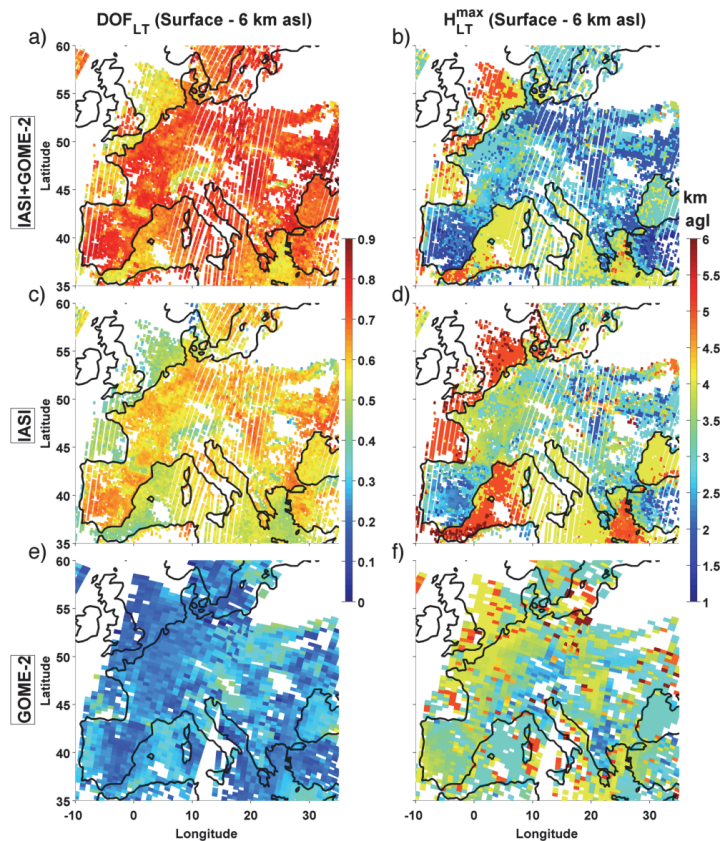
Fig. 4. Degrees of freedom DOF_{LT} (left) and heights of maximum AVK (km a.g.l.) H_{LT}^{max} (right) in the lower troposphere (LT, from the surface up to 6 km a.s.l.) for **(a,b)** IASI+GOME-2, **(c,d)** IASI only and **(e,f)** GOME-2 only ozone retrievals over Europe on 19 August 2009.

Lowermost tropospheric ozone by synergism of IASI and GOME-2

J. Cuesta et al.

Title Page

Abstract | Introduction

Conclusions | References

Tables | Figures

|◀ | ▶|

◀ | ▶

Back | Close

Full Screen / Esc

Printer-friendly Version

Interactive Discussion
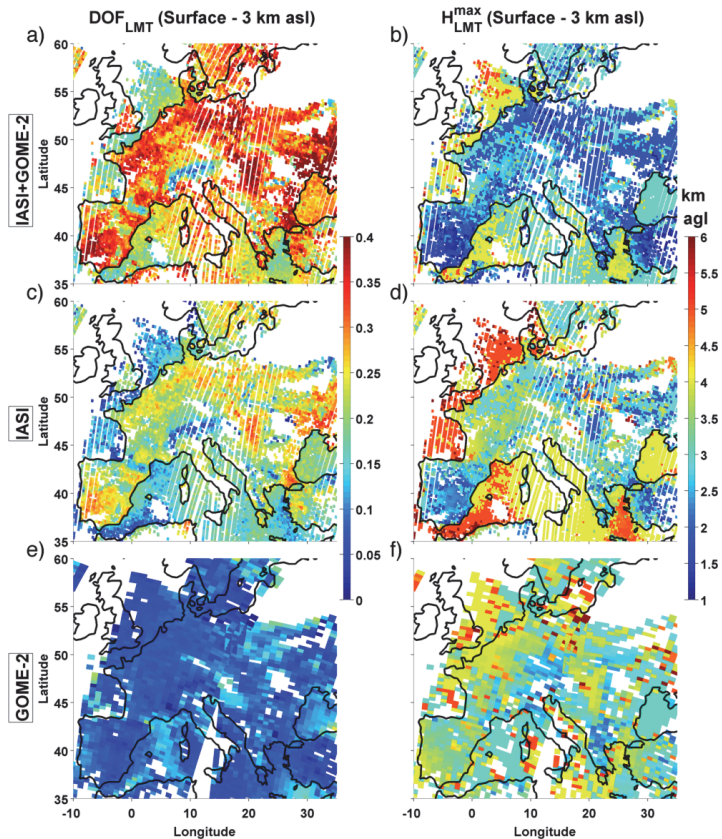
Fig. 5. Same as Fig. 4, but for the lowermost troposphere (LMT, from the surface up to 3 km a.s.l.).

Title Page

Abstract | Introduction

Conclusions | References

Tables | Figures

◀ | ▶

◀ | ▶

Back | Close

Full Screen / Esc

Printer-friendly Version

Interactive Discussion
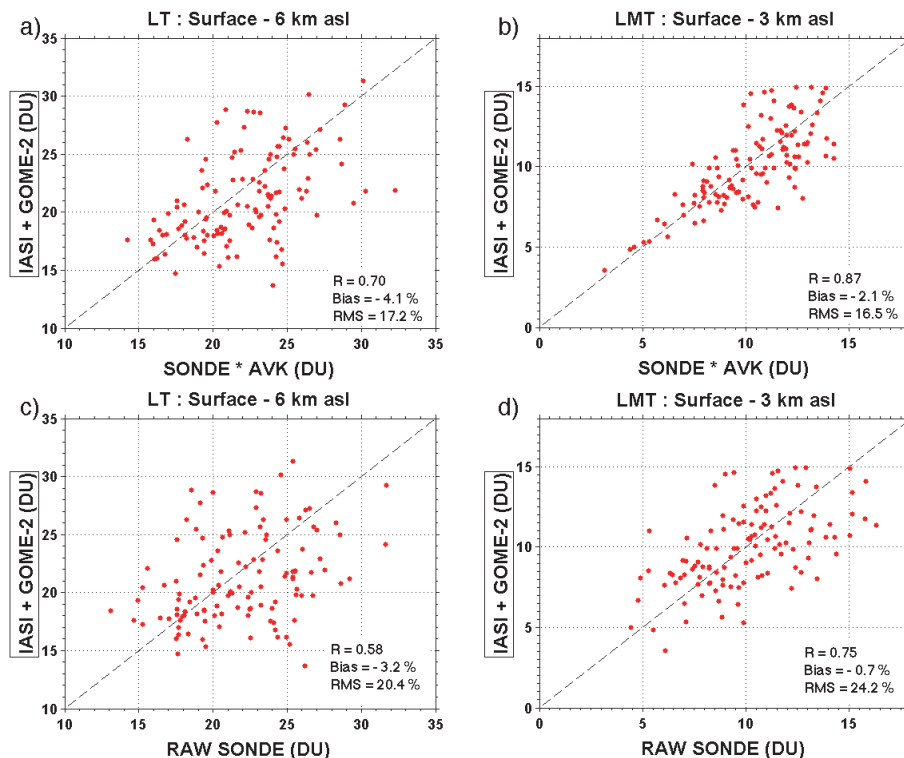
Fig. 6. Validation of IASI+GOME-2 ozone retrievals in the (**a** and **c**) lower troposphere (LT, up to 6 km a.s.l.) and (**b** and **d**) lowermost troposphere (LMT, up to 3 km a.s.l.) against ozonesonde measurements over Europe during the summer of 2009 (119 sondes launched from 10 stations during 57 different days). In upper panels **(a,b)**, ozonesonde are smoothed by IASI+GOME-2 AVKs and in lower panels **(c,d)**, raw ozonesonde measurements are considered. Dashed lines are straight lines crossing zero with slope equal to one.
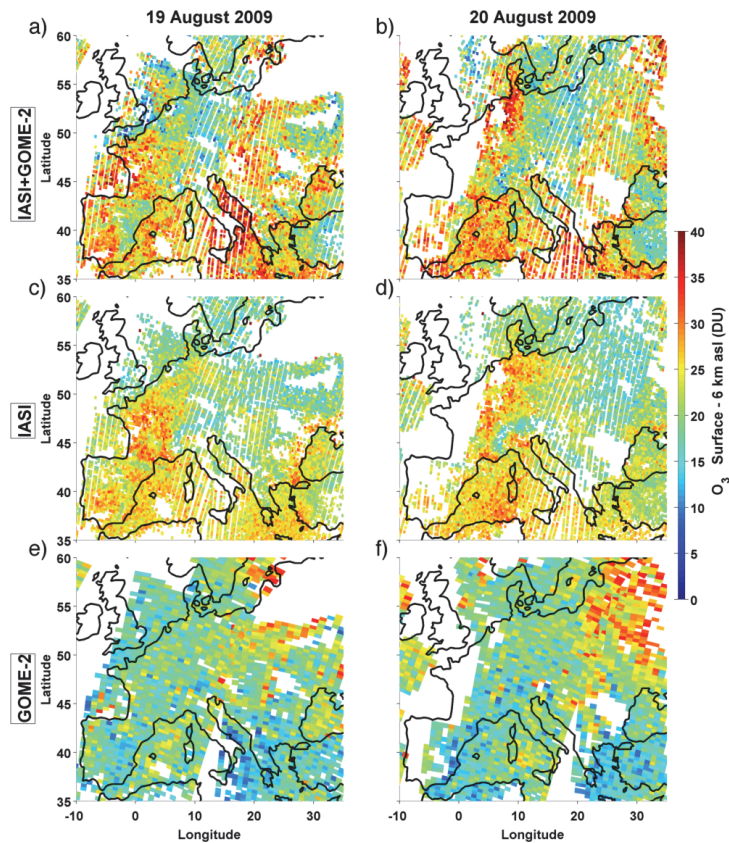
Fig. 7. Ozone observations (DU) in the lower troposphere partial column (LT, up to 6 km a.s.l.) over Europe on 19 (left) and 20 (right) August 2009 from **(a,b)** IASI+GOME-2, **(c,d)** IASI only and **(e,f)** GOME-2 only approaches.

Lowermost tropospheric ozone by synergism of IASI and GOME-2

J. Cuesta et al.

Title Page

Abstract | Introduction

Conclusions | References

Tables | Figures

◀◀ | ▶▶

◀ | ▶

Back | Close

Full Screen / Esc

Printer-friendly Version

Interactive Discussion
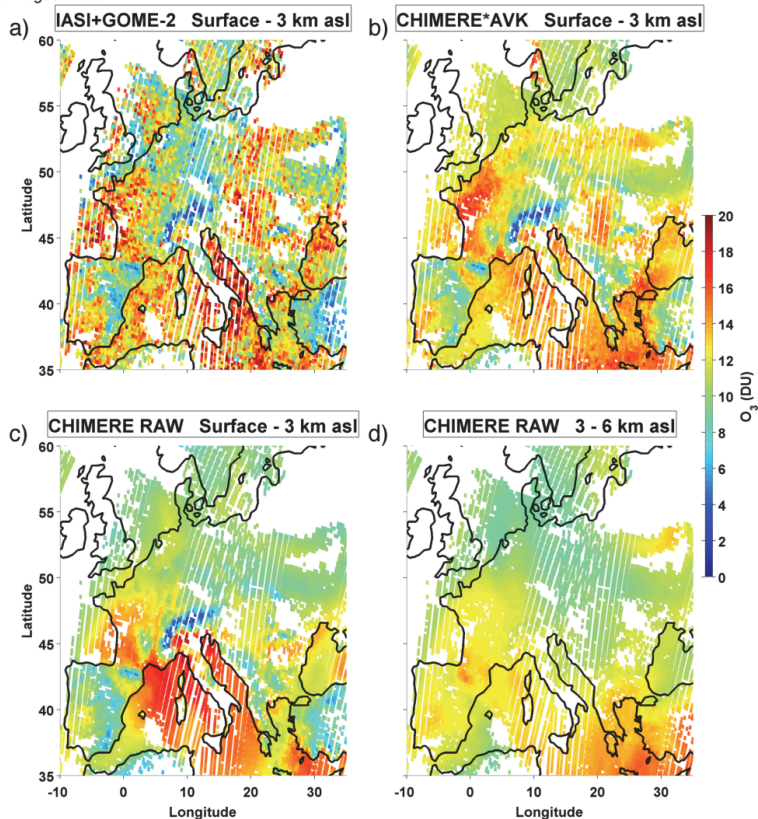
Fig. 8. (a) Ozone observations (DU) in the lowermost troposphere (LMT, up to 3 km a.s.l.) from IASI+GOME-2 multispectral approach over Europe on 19 August 2009. **(b)** CHIMERE model outputs in the LMT (up to 3 km a.s.l.) smoothed by IASI+GOME-2 AVKs. **(c)** CHIMERE raw outputs in the LMT. **(d)** CHIMERE raw outputs integrated between 3 and 6 km a.s.l.

Title Page

Abstract | Introduction

Conclusions | References

Tables | Figures

|◄ | ►|

◄ | ►

Back | Close

Full Screen / Esc

Printer-friendly Version

Interactive Discussion
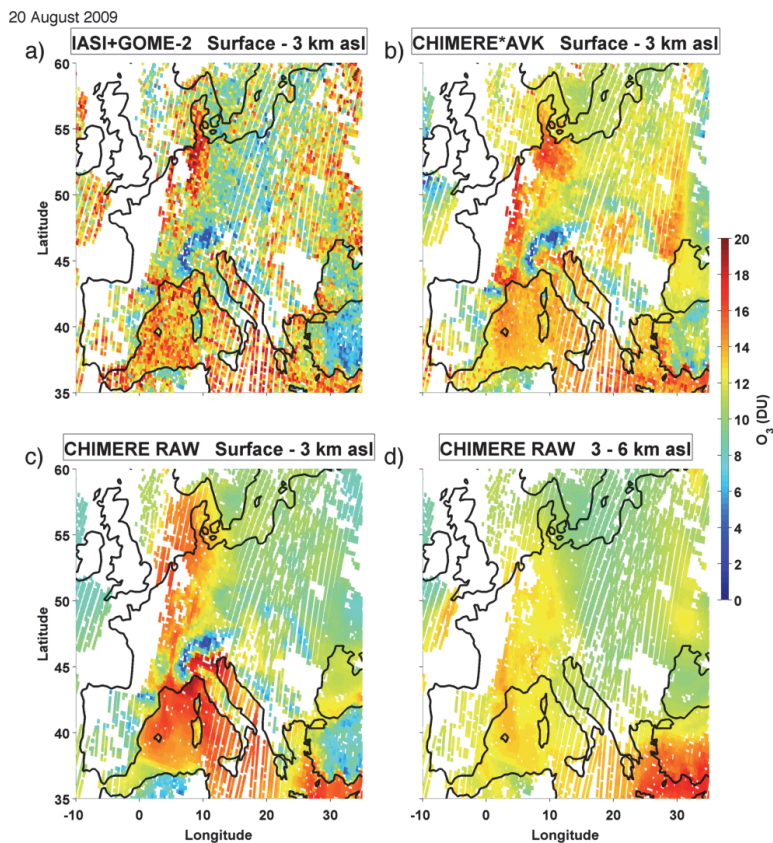
Fig. 9. Same as Fig. 8, but for 20 August 2009.

Discussion Paper | Discussion Paper | Discussion Paper | Discussion Paper

ACPD

13, 2955–2995, 2013

Lowermost tropospheric ozone by synergism of IASI and GOME-2

J. Cuesta et al.

Title Page

Abstract   Introduction

Conclusions   References

Tables   Figures

◀◀   ▶▶

◀   ▶

Back   Close

Full Screen / Esc

Printer-friendly Version

Interactive Discussion